Hybrid Beam-Steering OFDM-MIMO Radar: High 3-D Resolution With Reduced Channel Count

David A. Schneider⬤, Markus Rösch⬤, Axel Tessmann⬤, and Thomas Zwick⬤, *Fellow, IEEE*

Abstract—We report on the realization of a multichannel imaging radar that achieves uniform 2-D cross-range resolution by means of a linear array of a special form of leaky-wave antennas. The presented aperture concept enables a tradeoff between the available range resolution and a reduction in the number of channels required for a given angular resolution. The antenna front end is integrated within a multichannel radar based on stepped-carrier orthogonal frequency-division modulation, and the advantages and challenges specific to this combination are analyzed with respect to signal processing and a newly developed calibration routine. The system concept is fully implemented and verified in the form of a mobile demonstrator capable of soft real-time 3-D processing. By combining radio frequency (RF) components operating in the W-band (85–105 GHz) with the presented aperture, a 3-D resolution of less than $1.5° \times 1.5° \times 15$ cm is demonstrated using only eight transmitters and eight receivers.

Index Terms—Calibration, frequency scanning, millimeter-wave radar, multiple-input–multiple-output (MIMO), orthogonal frequency-division multiplexing (OFDM), stepped carrier.

I. INTRODUCTION

BANDWIDTH yields range resolution—this fundamental property of radar systems has driven the development of radio frequency (RF) components and the exploration of higher and broader frequency bands for more than five decades. Any sophisticated combination of modulation schemes, signal models, and processing algorithms shares this clear path toward increasing a system's ability to separate closely spaced reflectors.

As a direct result from the efforts in making autonomous driving a reality [1], resolving even thinner layers of material structures [2], or detecting tiny displacements in challenging industrial environments [3], radar transceivers with a usable bandwidth in the order of 10–50 GHz and an output power level suitable for midrange applications are becoming more and more widely available [4]–[6].
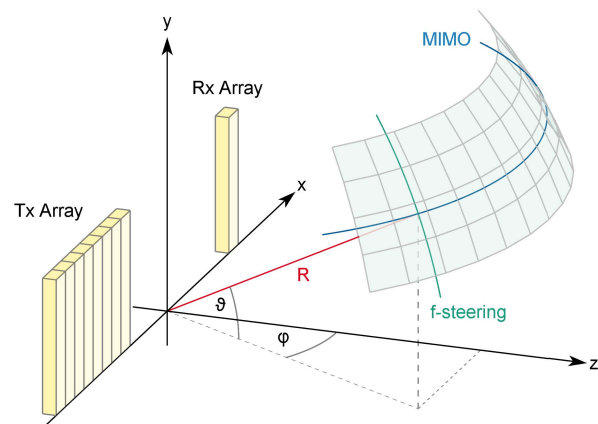
Fig. 1. Structural diagram of the proposed aperture and definition of the coordinate system. Both the Tx and the Rx antenna feature fan beam patterns that are narrow and frequency-steerable along the elevation ($\varphi = $ const) direction and wide in the azimuth ($\vartheta = $ const) direction.

At the same time, there are a growing number of applications that benefit from the capability to resolve targets in one or even two angular dimensions. This includes some of the technology drivers cited above, but also low-volume, high-cost applications in fields such as security and surveillance that require fast and precise coverage of angles often much less than a half-space [7]–[9].

Table I lists several techniques available to achieve a given angular resolution (or, equivalently, a given electrical aperture D/λ) as well as the number of active channels associated with their realization. If scanning speed or mechanical robustness plays a crucial role and the relative motion between the imaging system and target is not controlled, solutions based on mechanical steering or (inverse) synthetic aperture radar (SAR) are usually at a disadvantage. Broadband phased and/or reconfigurable arrays with a sufficiently high flexibility often require precise control over RF paths that are very hard to design and calibrate, especially for higher operating frequencies. This usually leaves techniques relying on the synthesis of multiple physical radar channels as the best remaining option.

Radar systems based on multiple-input–multiple-output (MIMO) arrangements have been successfully built and deployed, ranging from only a few to several thousand individual transmitters and receivers [10], [11], see also the extensive compilation by Kueppers *et al.* [12]. Unfortunately, full 2-D

TABLE I

METHODS FOR OBTAINING FAR-FIELD ANGULAR RESOLUTION

Method	Channel Count (best case)	Key Challenges
Mechanical scanning	$\mathcal{O}(1)$	Scanning speed, mechanical failure
2D phased/ reconfigurable arrays	$\mathcal{O}(1)$	Phase shifters, switching networks
(I)SAR	$\mathcal{O}(1)$	Inertial motion, scanning speed
2D MIMO	$\mathcal{O}(D/\lambda)$	Calibration, interference
Hybrid beam-steering (this work)	$\mathcal{O}(\sqrt{D/\lambda})$	Broadband front ends, aperture design, system integration

MIMO systems require a number of active channels that grows proportional to the targeted (linear) aperture D. Though this number can be reduced to some extent by trading angular resolution for sidelobe suppression in sparse and/or randomized arrangements [8], [10], [12], the asymptotic scaling remains the same. A high channel count is especially undesirable when high-performance technologies, such as those based on III–V semiconductors, are involved due to their high per-channel cost and nontrivial medium-scale integration or when baseband processing power is limited due to power or portability constraints.

If the operating bandwidth of the available hardware exceeds the application's requirements regarding range resolution, a situation becoming more and more widespread due to the technological advances mentioned above, an interesting tradeoff becomes possible in the design of these systems: Angular resolution can be increased at the cost of range resolution via exploiting frequency sensitive elements, usually antennas. The basic idea of this approach is to distribute the available bandwidth into multiple angular sectors without increasing the channel count.

So far, several 1-D radar systems based on a single [13], [14] or two orthogonally mounted frequency-scanning antennas [15] have been reported, but the geometrical shape and/or design bandwidth of the antenna elements prohibits their use as an element in a configuration that delivers a truly 3-D image with high angular resolution and high range resolution in the millimeter-wave regime.

A concept based on the combination of frequency-sensitive elements with a linear MIMO aperture was proposed by Orth et al. [16] based on simulations and later by Shoykhetbrod et al. [17] based on measurements of an artificially synthesized aperture. The reported antenna structure, however, based on cost-effective technologies and comprising omnidirectional receivers and geometrically large, resonant-slot transmitters, only allows for a moderate array directivity in the scanning plane (antenna gain is not given) as well as operating bandwidth and, correspondingly, combined angular/range resolution ($6.2° \times 10.2° \times 23$ cm simulated).

In this work, we take up on the idea of combining frequency-steering antennas with 1-D MIMO but instead propose the integration of recently developed, highly directive leaky-wave antennas (LWAs) with fan beam characteristics in the transmitting (Tx) and receiving (Rx) paths of a linear MIMO array, as shown in Fig. 1. As a result, the effectiveness and, consequently, the practical relevance of the hybrid frequency-scanning approach are significantly increased. By tailoring eight Tx and eight Rx channels operating in the W-band to the targeted array configuration, a uniform angular resolution of at least $1.5° \times 1.5°$ with a range resolution of 10 to 15 cm is achieved. For comparison, a classic 2-D MIMO array with a comparable angular resolution would require eight times as many active channels. This combined resolution allows the discretization of the scene into voxels that are potentially more suitable for many midrange imaging applications (e.g., 10–100 m) than approaches currently available.

To demonstrate the system integration of the proposed front end, we implement a multichannel stepped-carrier orthogonal frequency-division multiplexing (SC-OFDM) modulation scheme. OFDM radar is widely considered to be a promising technology for many spectrally dense scenarios requiring higher flexibility than conventional analog modulation [18], and several current hardware and algorithm development trends (e.g., in the fields of analog/digital converters, field-programmable logic, and sparse reconstruction techniques [19], [20]) are working toward eliminating the remaining obstacles to its widespread usage. For this reason, our detailed discussion of the steps necessary to integrate the presented aperture into such a system, covering aspects from signal processing to calibration algorithms, will hopefully prove valuable to future system designs.

The structure of the following reflects the key contributions of this work. In Section II, the details of the proposed antenna configuration are discussed. This encompasses resolution tradeoffs during design and operation as well as some special properties regarding MIMO ambiguity. While these aspects are largely independent of the actual radar modulation scheme, Section III is devoted to the integration of the aperture into an actual SC-OFDM radar and addresses its unique challenges, including the development of a suitable calibration routine. Section IV contains a short functional description of the realized system demonstrator that was used to obtain the system verification and real-world measurements presented in Section V.

II. APERTURE DESIGN CONCEPT

A. Overview

As an example of an idealized system-level view of the proposed aperture, consider the illustration in Fig. 2. For a given 2-D angular resolution λ/D and a range resolution $c/(2B)$, the classic, minimal T-shaped MIMO array shown on the left is one option, featuring $\mathcal{O}(D/\lambda)$ channels with a bandwidth B. On the basis of a frequency-steering antenna with a suitable 1-D directivity compatible to the required angular resolution and a combination of operating bandwidth B'

SCHNEIDER *et al.*: HYBRID BEAM-STEERING OFDM-MIMO RADAR

3

This article has been accepted for inclusion in a future issue of this journal. Content is final as presented, with the exception of pagination.
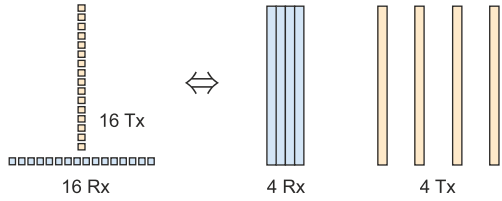

Fig. 2. Illustration of aperture equivalence between a T-shaped 2-D MIMO array (left) and a 1-D MIMO array of broadband frequency-steering antennas (right). Figuratively speaking, one angular dimension is redistributed along the bandwidth axis, leading to a reduction in the number of active channels.

and steering sensitivity σ compatible to the required sector coverage $\sigma B'$, the arrangement of $\mathcal{O}(\sqrt{D/\lambda})$ elements on the right is also possible. Though there are a number of differences between these two approaches regarding system integration as discussed next, they are completely equivalent from an imaging perspective, the frequency-steering antennas acting as a "translating element" between bandwidth and angular coverage. Between those two options, the primary cost tradeoff is a high number of channels on the one hand (left part) and a high operating bandwidth B' with potentially reduced coverage on the other hand (right part).

Obviously, the design of a "suitable antenna" as shown in Fig. 2 becomes harder with increasing angular resolution, as it involves the realization of compact but highly directive antennas for millimeter-wave frequencies. Thus, the relative number of elements that can be saved under the assumption of similar resolution requirements in both angular dimensions is a potential figure of merit of the antenna/aperture design, in this work amounting to

$$\text{FOM}_1 := \frac{2N_{\text{Tx}}N_{\text{Rx}}}{N_{\text{Tx}} + N_{\text{Rx}}} \approx \frac{4}{(N_{\text{Tx}} + N_{\text{Rx}})\delta\varphi} \approx 8. \tag{1}$$

The hybrid aperture considered here consists of a linear array of frequency-steering elements with fan beams, lined up along the x-axis as shown in Fig. 1. Note that all further derivations assume far-field conditions, so the position of the depicted, extended antennas along the y-axis is arbitrary to some extent and has been chosen for visual clarity, while the effective center of the overall aperture is always assumed to coincide with the origin of the coordinate system. As will become apparent during the discussion, the given choice of the spherical coordinates ϑ and φ naturally reflects the structure of the fan beam pattern in combination with a wideband MIMO array and introduces the least amount of coupling between the coordinates during data processing.

On the basis of a target bandwidth of 20–25 GHz and imaging applications covering ranges from about 5 to 100 m, devising Tx and Rx elements that "play well" with array integration on the one hand and the relatively high operating bandwidth, on the other hand, is the design challenge affecting overall system performance the most.

B. Antenna Elements

A single-frequency-steering antenna element should have fan beam characteristics, i.e., a narrow, frequency-scanning beam along $\varphi = $ const combined with a broad beam along $\vartheta = $ const. There are N_{Tx} transmitters and N_{Rx} receivers,

arranged in a classic linear MIMO array along the x-axis with receiver spacing d and transmitter spacing $N_{\text{Rx}}d$. This leads to a virtual array size of

$$D_\varphi = N_{\text{Tx}}N_{\text{Rx}}d \tag{2}$$

and the corresponding resolution

$$\delta\varphi = \frac{\lambda}{D_\varphi} = \frac{\lambda}{N_{\text{Tx}}N_{\text{Rx}}d} \tag{3}$$

in the azimuth direction, while the effective resolution in the elevation direction is given by the narrow beamwidth $w_{3\,\text{dB}}$ of the (Tx and Rx combined) fan beam

$$\delta\vartheta = w_{3\,\text{dB}} = \sigma B_{3\,\text{dB}}. \tag{4}$$

The second equality, where σ denotes the steering sensitivity of the fan beam, holds under the pragmatic assumption that the full antenna pattern $P(f, \vartheta)$ does not change much over the operating bandwidth (apart from the steering effect). As a consequence, we will assume for the sake of the calculation that its functional shape p is essentially the same for a fixed elevation as it is for a fixed frequency, i.e.,

$$P(f_0, \vartheta) = p(\vartheta - \sigma f_0) = p(\sigma(f - f_0)) \tag{5}$$

where p features a full-width at half-maximum (FWHM) of $w_{3\,\text{dB}}$ and axial symmetry with respect to its (only) argument.

As shown in Fig. 2, antenna elements fulfilling

$$w_{3\,\text{dB}} \approx \delta\varphi = \frac{\lambda}{N_{\text{Tx}}N_{\text{Rx}}d} \tag{6}$$

while scanning the required elevation interval over their operating bandwidth can be used to synthesize an aperture from $N_{\text{Tx}} + N_{\text{Rx}}$ elements that is equivalent to a 2-D MIMO aperture of $2N_{\text{Tx}}N_{\text{Rx}}$ elements in terms of angular resolution. The case $N_{\text{Tx}} = N_{\text{Rx}}$ is optimal with respect to the total channel count and will be considered from this point on.

In order to meet (6) for a value of N as large as possible, an antenna array is developed based on a class of narrow-wall LWAs recently introduced by Schneider *et al.* [21]. In contrast to previous approaches, it neither relies on resonant slots (thus, increasing the relative operating bandwidth to more than 25%) nor on continuous openings (enabling the small leakage factors necessary to realize its large physical dimension of approximately 60λ.) The nature of the small narrow-wall openings also allows for the integration into an Rx array with a spacing of $d = 2.5$ mm without introducing significant mutual couplings between the antennas.

The fundamental waveguide mode (Floquet index $n = 0$) is radiated, so the elevation coverage is tilted toward the endfire direction (see Figs. 1 and 3), and both the transmitter and the receiver show almost perfect linear polarization (combined isolation greater than 60 dB) along the φ-direction. The resulting aperture gain is shown in Fig. 3; a picture of the antenna hardware as part of the RF front end is included in the left of Fig. 9.

The shaded area in the left of Fig. 3 shows the elevation coverage of the steered beam, which is limited in our case by the RF hardware of the demonstrator to about $18°$ with a steering sensitivity of approximately $0.8°\,\text{GHz}^{-1}$ over the operating bandwidth from 85 to 105 GHz. The ratio of the

This article has been accepted for inclusion in a future issue of this journal. Content is final as presented, with the exception of pagination.

4   IEEE TRANSACTIONS ON MICROWAVE THEORY AND TECHNIQUES
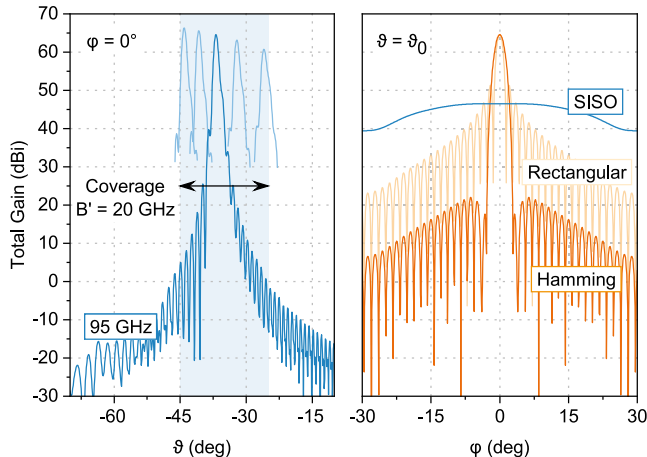

Fig. 3.   Total aperture gain (Tx, Rx, and MIMO) in elevation (left) and azimuth (right) direction, based on electromagnetic (EM) simulations of the antenna structures and an MIMO array factor for 64 virtual elements with a rectangular/Hamming window. The curve labeled "SISO" shows the azimuth coverage of a single transceiver without the additional MIMO processing gain. The change in the elevation pattern over an operating bandwidth from 85 to 105 GHz is indicated in the left.

elevation coverage and the (average) FWHM is a figure of merit associated with an individual combination of Tx and Rx antennas and thus useful in assessing the suitability of a given antenna design for the integration into a hybrid aperture. For the design presented in this work, we find

$$\text{FOM}_2 := \frac{\sigma B'}{w_{3\,\text{dB}}} \approx 18 - 20 \qquad (7)$$

depending on whether the active components or the antenna itself is considered to be the limiting factor of B'.

The elevation pattern shown in Fig. 3 is tailored during aperture design by varying the leakage constant of the LWAs in a suitable way but cannot be changed afterward. For more details on the design procedure, manufacturing process, and simulation model of the single antenna elements, we refer to our previous work [21].

The right shows a pattern cut at $\vartheta = \text{const}$ for a single combination of transmitter and receiver [single-input single-output (SISO)] as well as for the full MIMO array with two exemplary weighting functions: a rectangular and a Hamming window. This part of the array synthesis is performed virtually, so the entire toolbox of beamforming techniques [22] is in principle applicable here. The space $N_{\text{Rx}}d$ available between the transmitters is filled with flaring (horn-like) structures, which increases the directivity of the fan beam in the plane perpendicular to the steering action. The effect is visible in the SISO curve in Fig. 3 and used in conjunction with the elevation tilt to suppress grating lobes appearing at large azimuth angles due to $d > \lambda/2$.

In the following, several aspects are discussed, which are central to the imaging performance of the aperture.

C. Range/Elevation Resolution

In every frequency-scanning radar with a given operating bandwidth, there is an obvious tradeoff between angular

coverage, angular resolution, and range resolution or "illumination bandwidth." While the first two are usually chosen in the design stage, a certain degree of flexibility or adaptivity remains during operation in the choice of the coherently integrated bandwidth B as discussed in this section. As this effect is situated in the R, ϑ dimensions, and thus independent of the MIMO array geometry, we restrict the argument to a single combination of transmitter and receiver.

Consider the complex spectral response function $h(f)$ of a single isotropic point target at range R_0 and elevation ϑ_0, i.e.,

$$h(f) \propto \exp\left(-2\pi j \frac{2R_0}{c} f\right) p(\sigma f - \vartheta_0). \qquad (8)$$

For example, h can be interpreted as the intermediate frequency (IF) signal of a frequency-modulated continuous-wave (FMCW) radar or the channel transfer function obtained by an OFDM radar, both encoding the target range in a phase proportional to its argument. Without any specific assumptions about the structure of the underlying scene, the following short-time Fourier transform (STFT) yields the optimal range/angle compression on an equidistant grid:

$$\pi_B(R, \vartheta) := \int_{\vartheta/\sigma - B/2}^{\vartheta/\sigma + B/2} e^{2\pi j \frac{2R}{c} f} h(f) df. \qquad (9)$$

To obtain the imaging resolution in range and elevation directions, two cuts are evaluated around the true target position R_0 and θ_0, respectively

$$|\pi_B(R_0, \vartheta_0 + \Delta\vartheta)| = \left| \int_{\Delta\vartheta/\sigma - B/2}^{\Delta\vartheta/\sigma + B/2} p(\sigma f) df \right| \qquad (10)$$

$$|\pi_B(R_0 + \Delta R, \vartheta_0)| = \left| \int_{-B/2}^{B/2} e^{2\pi j \frac{2\Delta R}{c} f} p(\sigma f) df \right|. \qquad (11)$$

In Fig. 4, the FWHM of both cuts is visualized as a function of the integration bandwidth B. Solely for the purpose of illustrating the influence of the antenna phases on the result, the same calculation is performed after replacing p by $|p|$ in both cuts; the result is drawn with a dotted line. For comparison, the theoretical limit of the range resolution

$$\delta R_{\min} = \frac{c}{2B} \qquad (12)$$

is also included. The inset shows the form of (10) for various bandwidths, which can be interpreted as an "effectively broadened antenna pattern" caused by the integration of p over a finite interval around the true target elevation (steering frequency). In (11), on the other hand, p takes the role of a windowing function to the constant integrand 1, smoothly cutting off an increasing portion of h as B increases.

The practical relevance of Fig. 4 lies in the fact that B is only a parameter of the processing algorithm, so, within certain limits, both range and elevation resolutions can be adjusted to the requirements regarding target separation during operation or postprocessing.

D. Azimuth Resolution and Ambiguity

While the phase relations between virtual receivers and the occurrence of ambiguities in the MIMO array factor are well-understood phenomena, two properties of the presented aperture cause an additional, more subtle effect that is discussed in
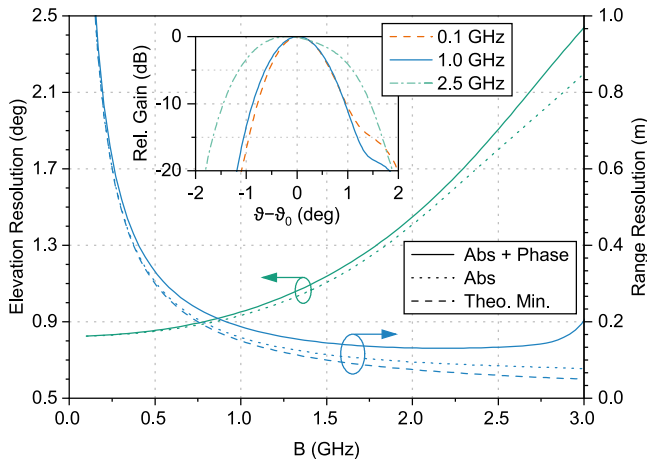
Fig. 4. Main Panel: range and elevation resolution as a function of the coherently integrated bandwidth B. When the full complex antenna pattern is considered, destructive interference effects decrease the resolutions. The theoretical limit for the range resolution is given by $c/(2B)$. Inset: Effective antenna patterns in the scanning plane for different values of B.

Fig. 5. MIMO/frequency interaction. The variation of the electrical length d/λ is compensated by the frequency-steering term $\cos\vartheta$, leading to flat azimuth resolution and ambiguity regions over the operating bandwidth.

this section: the influence of the frequency-steered elevation on the MIMO ambiguity function, and its interaction with a relative operating bandwidth of more than 20%, i.e., the varying electrical separation of the virtual elements.

From the definition of the coordinate system in Fig. 1, the relative phase of a signal with wavelength λ, impinging on the virtual receiver $n \in \{0, \ldots, N^2 - 1\}$, can be calculated under far-field conditions to

$$\Phi_n = n \cdot 2\pi \frac{d}{\lambda} \underbrace{\cos\vartheta \sin\varphi}_{x/R} . \tag{13}$$

The angular resolution of the array is basically determined by the phase resolution $\delta\Phi_n$ (number of elements, aperture size), and its first grating lobes are given by the phase ambiguities $\Phi_n \equiv \Phi_n \pm 2\pi$.

Both the electrical separation of the antenna elements d/λ and the steering factor $\cos\vartheta$ vary as a function of the operating bandwidth, as shown in Fig. 5. For this particular antenna, the amount of these variations is chosen to be approximately equal, but with opposite signs. As a result, the azimuth resolution

$$\delta(\sin\varphi) = \frac{\lambda}{2\pi nd \cos\vartheta} \delta\Phi_n \propto \frac{1}{N^2} \tag{14}$$

and the two critical angles

$$\sin\varphi_1 = \frac{\lambda}{d \cos\vartheta} - 1 \tag{15}$$

$$\sin\varphi_2 = \frac{\lambda}{2d \cos\vartheta} \tag{16}$$

remain almost constant over the entire operating bandwidth. φ_1 and φ_2 define the three angular regions visualized in Fig. 5 that are present in any MIMO array with $\lambda > d > \lambda/2$.

In the unambiguous region, there is a one-to-one correspondence between the true target elevation and the detected phase shifts, i.e., a single virtual main lobe. Due to the phase ambiguity, targets with a true elevation in the mirrored region appear mirrored into the region of the first grating
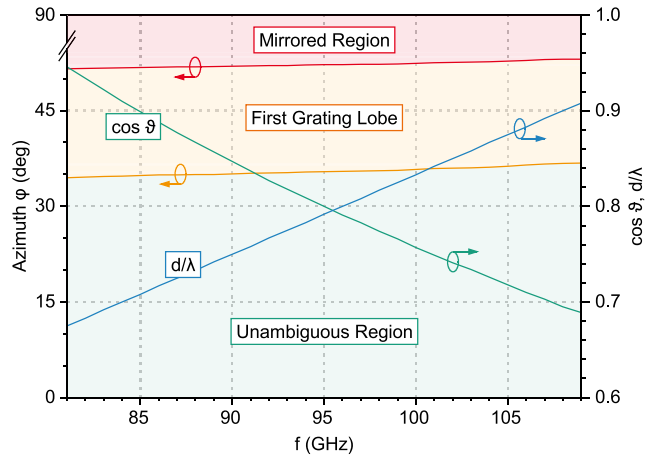
lobe, together with targets whose true elevation falls in this region and is correctly estimated. In the presented design, this problem is solved by means of the additional flaring/horn structures briefly mentioned above, decreasing the grating lobe of the array factor to an acceptable level.

Note that (14)–(16) are not in contrast to the intuitive statement that a variation of the electrical aperture always corresponds to a variation of the imaging resolution in that dimension, regardless of the mechanism of angular coverage. While a classic, narrowband array maintains a constant imaging resolution $\delta(x/R)$, the discussed aperture is designed in such a way that the combined effects of broadband operation and frequency steering yield a constant azimuth resolution $\delta\varphi$, instead of merely an uncontrolled variation of the former expression. As a useful matter of fact that can be exploited during signal processing, this decouples the elevation and azimuth coordinates (only) for the presented choice of coordinate system.

E. Signal-to-Noise-Ratio Considerations

As the presented aperture basically replaces a full 2-D MIMO arrangement by a number of spectrally disjoint linear arrays, it is also less susceptible to some of the former's weaknesses.

In theory, 2-D MIMO and the proposed aperture are equivalent in terms of signal-to-noise ratio (SNR) as (physical) antenna gain is replaced by (digital) processing gain or vice versa. In practice, however, 2-D MIMO apertures only harness their full potential when perfectly and stably calibrated, which is not always easy to achieve. In the proposed design, only one dimension (azimuth) needs to be calibrated, and this process can be performed incrementally, i.e., once per elevation sector (see Section III-D); the price for this increased robustness is a fixed pattern in the frequency-steering direction.

Another situation where the hybrid approach might prove beneficial is the presence of strong localized reflectors or other scenes with an exceptionally high dynamic range (e.g., combined ground/air coverage). While a single reflector may

suffice to completely "blind" a 2-D MIMO aperture due to compression of the low-noise amplifier (LNA), only a potentially small elevation interval would be affected in the hybrid design as the elevation filtering (via frequency scanning) is happening before the signal reaches the first active component.

III. HYBRID FREQUENCY-STEERING AND OFDM RADAR

In this section, the basic signal model of an SC-OFDM radar is summarized. A more detailed discussion of those aspects that are specific or need to be tailored to the hybrid aperture concept, i.e., 2-D angular processing, follows. As any real system shows a number of deviations from the transfer characteristics on which the SC-OFDM signal model is based, the most prominent of these nonidealities is addressed in Section III-D. In this context, two complementary calibration schemes are developed, dealing with the IF and RF part of the transfer function, respectively. Both schemes take advantage of the presented aperture concept and allow for a potentially more robust realization than standard approaches applied to an equivalent 2-D array.

A. Introduction to SC-OFDM Radar

From a modern radar perspective, OFDM offers a spectrally efficient way of sampling the transfer function h of a channel between a transmitter and a receiver. Either as a central feature or as a side effect, it allows for a seamless integration of channel sounding (i.e., radar) and the transmission of payload data (communication) into a single modulated waveform, which is an attractive concept that has been thoroughly investigated under keywords such as RadCom [23], [24].

While the first processing schemes were based on the application of matched filters to the OFDM waveform in the time domain [25], consequently suffering from the usual drawbacks associated with baseband correlation, it was shown by Sturm *et al.* [26] that algorithms operating directly in the symbol domain exploit the subcarrier orthogonality in a more efficient way, thus offering superior radar performance in many scenarios.

As OFDM requires handling, especially sampling, the full RF bandwidth in the baseband (in contrast to, e.g., FMCW radar), several techniques have been developed to avoid sampling the full channel function at once, e.g., by exploiting the properties of nonequidistant frequency combs [27] or coherently combining data obtained from transmissions with different carrier frequencies. The latter approach, called SC-OFDM, was first demonstrated by Pfeffer *et al.* [28] and significantly improved by Schweizer *et al.* [29], [30] with respect to the robustness and ambiguity of the coherent phase processing involved. As there is a natural correspondence between elevation and frequency sectors for the antenna elements proposed in this work, SC-OFDM and the hybrid aperture concept benefit from each other in multiple ways.

B. Signal Model

As its name suggests, SC-OFDM radar obtains the information about h by sending and Rx a number of OFDM

symbols with varying carrier frequencies f_k, $k = 1, \ldots, N_c$ and complex payload data p_l. The standard OFDM baseband model takes the form

$$x_{\text{Tx}}(t) = \sum_{l=0}^{N_s-1} p_l \exp(2\pi j l \beta t) \qquad (17)$$

together with the orthogonality condition

$$N_s \beta = f_s \qquad (18)$$

relating the sampling rate f_s to the subcarrier spacing β. The channel function is obtained by dividing the received data p_l' by p_l; in a radar-only context, the complex p_l are usually distributed on the unit circle to maximize SNR with their phases chosen according to some sequence that minimizes the peak-to-average power ratio (PAPR) of $x_{\text{Tx}}(t)$ (see the survey by Han and Lee [31]).

For the linear MIMO array shown in Fig. 1, this process is repeated for each virtual receiver i and carrier frequency f_k. Assuming a general, nondispersive distribution of reflectors $\rho(\vec{r})$ in the imaging space Ω, this yields the following model for the transfer function, evaluated at the spectral position of the n-th subcarrier:

$$h_{ik}(n) = \int_{\Omega} \rho(\vec{r}) \exp(j\Phi_0 + j\Phi_R + j\Phi_\varphi) d^3r \qquad (19)$$

where Φ_0 absorbs terms that do not depend on i, k, or n, and the other two phase terms linearly encode the relevant reflector properties R and $\sin\varphi$ in the following way:

$$\Phi_R(k, n) = -4\pi R \frac{f_k + n\beta}{c} \qquad (20)$$

$$\Phi_\varphi(i, k) = 2\pi \frac{f_k}{c} d \cos\vartheta \sin\varphi \cdot i. \qquad (21)$$

Note that due to the construction of the frequency-steering antennas, the dependency of Φ_φ on ϑ is very weak (cf. Section II-D), so the elevation information is not encoded in the phase.

By repeating the sampling process multiple times, a fourth term appears, corresponding to a slow-time phase progression that is proportional to the target's radial velocity. It allows for a Doppler evaluation similar to schemes based on fast chirp sequences [32]. For notational clarity, this additional dimension (index) is omitted as it does not interact with the aspects highlighted in this work.

If the carrier frequencies f_k are chosen according to

$$f_{k+1} = f_k + N_s \beta \qquad (22)$$

a single broadband OFDM symbol may be constructed from a number of subsymbols, significantly reducing the required sample rate for a given system bandwidth. Note that in practice, there will be a number of guard (zero) subcarriers p_k that lead to adjustments in the carrier step width but are otherwise irrelevant to the argument.

Without any further assumptions about the reflector distribution, a plausible reconstruction of ρ is based on a matched filter, applied to the measured transfer function h'

$$\rho'(R, \varphi) := \sum_{i,k,n} \underbrace{e^{-j\Phi_R(k,n) - j\Phi_\varphi(i,k)}}_{E(i,k,n)} h_{ik}'(n). \qquad (23)$$

By inspection of (19) to (21), it becomes clear that this matched filter takes the convenient form of a number of (inverse) Fourier transforms if the virtual array is equidistant and the (total) bandwidth is still small compared to the carrier frequency. Most system properties of SC-OFDM, such as range resolution, azimuth resolution, and the maximum unambiguous range, are a direct consequence of the basic properties of these Fourier transforms.

The last aspect of the SC-OFDM signal model relevant to this discussion concerns the transmission of orthogonal waveforms (multiplexing). Beside simple time-division multiplexing, which is suboptimal in terms of transmit power distribution and dynamic targets, OFDM radar also allows for the simultaneous operation of all transmitters. The two most prominent options are based on code multiplexing [33] and equidistant subcarrier multiplexing [34]. Both methods have their disadvantages, as code lengths increase with the number of transmitters, cross-correlation properties of code sequences are not ideal, and standard equidistant subcarrier allocation reduces the unambiguous range (i.e., the number of subcarriers available to each virtual transceiver) by a factor of N_{Tx}. The latter can be alleviated to a certain extent by randomizing (or optimizing) the subcarrier allocation [35], trading unambiguous coverage for sidelobe levels, similar to the synthesis of sparse arrays.

In this work, the equidistant subcarrier multiplexing scheme is used for its simplicity. As a consequence, h is sampled at regular frequency intervals that are slightly shifted against each other. Obviously, this effect is relevant during MIMO processing that is based on phase differences between virtual receivers. Thus, the shift needs to be compensated, either before range compression by inserting zeros at the subcarrier positions allocated to the other transmitters or, potentially more efficiently, by keeping only the nonzero part of h and performing the required fractional cyclic shift in the time-domain data by adding a range-dependent phase

$$\Phi_{\text{comp}} := 2\pi j \frac{2R\beta}{c} i_{\text{Tx}} \tag{24}$$

to all virtual receivers derived from transmitter i_{Tx} after the Fourier transform. It can be shown that both variants equivalently lead to a perfect compensation of the phase shift at the points of maximum correlation, i.e., target peaks, see the analysis by Multerer *et al.* [36] for more details.

C. Elevation Processing

The main difference between the standard SC-OFDM model and the setup proposed in this work is the presence of an additional, frequency-steering dimension. As a consequence, the transfer function not only carries information about the target range and 1-D MIMO phase via its phase progression as a function of n and i, respectively, but also about the target elevation via masking (i.e., antenna pattern) of its absolute value, also as a function of n. On an equidistant grid, this separation problem in n can be efficiently addressed by means of a short-term Fourier transform as already anticipated in (9) if we associate $f \sim \beta n$.

As discussed in Section II-C, the central processing parameter is given by the coherent integration bandwidth B. In this context, it is synthesized by the combination of K subsymbols via

$$B = K N_s \beta. \tag{25}$$

To obtain the full radar image, we combine (9) in its discrete formulation with (23)

$$\rho'(R, \varphi, \vartheta) = \sum_{i,n} \sum_{k=k_-}^{k_+} E(i, k, n) h'_{ik}(n) w_R(k, n) w_\varphi(k, n) \tag{26}$$

where $k_\pm := \vartheta/\sigma \pm B/2$. Note that the ϑ-sectors are chosen in such a way that the corresponding summation limits are integers. Variations in σ over the full operating bandwidth can also be compensated at this point by replacing the linear approximation in $k_\pm$ with a suitable reference measurement $k(\vartheta)$. w_R and w_φ denote additional windowing functions in range and azimuth direction that provide the usual tradeoff between main lobe width (resolution) and sidelobe levels in the respective dimension.

The reconstruction scheme given in (26) is used to obtain the radar plots presented in this work. The grid on which ρ' is evaluated can be interpolated by employing zero padding in the i and n dimension; with the exception of the resolution verification, where no windowing is used, w_R and w_φ are implemented as Hamming windows of a suitable length.

If ρ' is not presented to the user in the form of a high-resolution image but instead used as the starting point for more advanced target detection or classification algorithms, a choice of w_R that tapers off with a cosine shape over the length of the overlap between adjacent ϑ sectors represents a particularly effective option as it completely preserves the original signal energy without introducing any additional redundancy.

Two aspects should be noted regarding the influence of the hybrid aperture on SC-OFDM processing. First, the narrowband assumption enabling the realization of the matched filter in (23) as a number of Fourier transforms is relaxed in (26) to the assumption that B (as opposed to the total operating bandwidth) is small compared to the carrier frequencies f_k. Thus, the hybrid aperture enables a broadband extension of the OFDM scheme without affecting the efficiency or validity of the narrowband signal processing within each elevation sector.

Second, SC-OFDM requires the coherent integration of all samples, respecting carrier steps as well as slow-time repetitions (in the case of full-range/Doppler processing). Depending on the velocity distribution of the radar scene, this imposes a certain limit on the maximum acceptable measurement time due to the occurrence of ambiguities and migration effects. This limit analogously only applies to the time spent covering B, instead of B'.

In summary, the increase in operating bandwidth required to achieve elevation coverage in the hybrid concept can be made largely transparent to the baseband signal processing.

D. System Calibration

For the stepped-carrier scheme to work in the simple way described in Section III-C, h is assumed to equal the channel

This article has been accepted for inclusion in a future issue of this journal. Content is final as presented, with the exception of pagination.

8

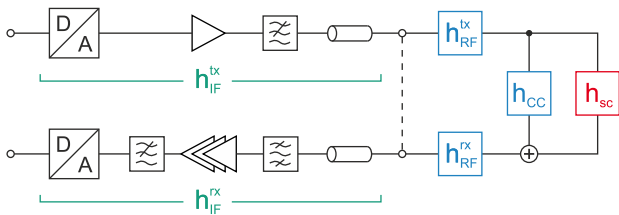IEEE TRANSACTIONS ON MICROWAVE THEORY AND TECHNIQUES

Fig. 6. Structure of the system transfer function H containing IF signal conditioning, RF components and cross coupling, as well as the actual radar scene h_{sc}. An additional IF loopback connection used for calibration is marked with a dashed line.

transfer function h_{sc} of the radar scene, i.e., it represents the physical paths between the Tx and the Rx antenna. In reality, however, all signal processing only has access to the full system transfer function H that contains several unwanted contributions. Fig. 6 shows a number of these additional contributions that are considered in the linear error model of this work.

The nonideal parts of the system transfer function can be divided into two categories. First, there are terms appearing in the baseband processing chain, i.e., before upconversion in the transmitter and after downconversion in the receiver, shown in the left of Fig. 6. These parts are captured by a combined transfer function $h^{IF}(n)$ that neither depends on k (stepping of the RF carrier) nor on i, assuming that individual tolerances between matched components in different virtual receiver paths are small compared to the overall response.

Second, the RF components (mixers, amplifiers, antennas, and interconnects) introduce additional error terms that potentially depend on all three indices i, n, and k. As the electrical dimensions of manufacturing tolerances are much larger in the RF part of the system, even carefully matched components introduce phase offsets that cannot be neglected during MIMO processing, so this part of the response is modeled by a transfer function of the form $h_{ik}^{RF}(n)$.

Reflecting this structure, we propose a two-part calibration procedure for the hybrid aperture SC-OFDM radar system. First, the baseband part is addressed. The fact that h_{IF} is independent of the carrier frequency leads to a violation of the "seamless transition condition" between subsequent subsymbols

$$H_{ik}(N_s - 1) \neq H_{ik+1}(0). \tag{27}$$

As this mismatch is periodic in the combined subcarrier index, severe artifacts are introduced during range compression. These detrimental effects have already been observed in a standard SC-OFDM setup by Schindler *et al.* [37]. With the aim of restoring the continuity of H, the authors devise a calibration apparently based on the assumption of a flat Tx–Rx cross coupling h_{cc}, exploited by zeroing the actual radar channel with an RF absorber placed on top of the antennas and subsequently dividing by this reference measurement. As the geometrical dimensions of our antenna elements and their immediate surroundings (radome) are in the order of the range resolution, this approach is not applicable here.

Instead, we propose a two-term error model for the IF channel function

$$h^{IF}(n) \sim e^{-2\pi jn\beta\tau} \cdot h_{LB}(n). \tag{28}$$

h_{LB} contains most of the filter and IF amplifier effects and is obtained by a loop-back measurement along the path shown in Fig. 6, averaged over all virtual channels. The remaining parameter τ is optimized with the goal of minimizing the discontinuity in (27) at the subsymbol boundaries, starting from a theoretical estimate based on processing delays and cable lengths. As the dominating effects of the IF channel response causing nonlinear phase response are captured in the second term, this scheme is found to remove artifacts due to IF periodicity over a wide dynamic range (see Section V-A).

The second part of the proposed calibration routine aims at eliminating phase differences between virtual receivers. It is based on the standard procedure of measuring the phases received from a reference reflector at $\varphi = 0$, which is, however, not directly applicable due to the highly directive, frequency-dependent elevation coverage. If we assume that h^{RF} changes only slowly over the bandwidth of K subsymbols, i.e.,

$$h_{ik+K}^{RF}(n) \approx h_{ik}^{RF}(n) \approx h_{ik}^{RF}(0) =: h_{ik}^{RF} \tag{29}$$

an estimate of the error term can be obtained via

$$h_{ik}^{RF} \sim \sum_{n=0}^{N_s-1} e^{-j\Phi_R(i,k,n)} h_{ik}(n) \tag{30}$$

where R denotes the range of a reference reflector estimated by the range compression filter (potentially combining a number of subsymbols). A very useful consequence of this result is the fact that the MIMO angle calibration can be done and repeated independently for all subsymbols k and without *a priori* knowledge of the synthesized bandwidth B or K, respectively. For example, the elevation interval could either be covered by moving a single reference target and constructing the calibration function in an incremental fashion or an extended calibration target such as a rod made of a number of trihedral reflectors could be installed once in the scene, and the calibration could be performed in a single measurement. The full calibration routine then takes the form

$$h'_{ik}(n) = \frac{\left(h_{ik}^{RF}\right)^*}{\left|h_{ik}^{RF}\right|} \cdot \frac{1}{h^{IF}(n)} \cdot H_{ik}(n) \tag{31}$$

with the additional, pragmatic restriction [as justified by (29)] that the same h_{ik}^{RF} is applied to all subsymbols k belonging to the same symbol synthesized from KN_s subcarriers.

Note that in terms of the full MIMO channel matrix, only corrections to the diagonal entries are considered here, i.e., mutual coupling between antennas is assumed to be either sufficiently small (based on field simulations within the Tx/Rx array) or easily accounted for by filtering targets with near-zero range (coupling between Tx and Rx array). Due to the digital range processing, the second effect still needs to be reduced to a level that does not limit the dynamic range of the receiver, which is achieved in the demonstrator system by a suitable combination of array placement, antenna opening

This article has been accepted for inclusion in a future issue of this journal. Content is final as presented, with the exception of pagination.

SCHNEIDER *et al.*: HYBRID BEAM-STEERING OFDM-MIMO RADAR

9

Fig. 7. Photograph of the realized demonstrator in a mobile rack, comprising the RF front end (black enclosure) on a steerable mount opposite the user interface, custom IF interfacing hardware, a standard personal computer, and a commercial dc power supply unit (PSU).
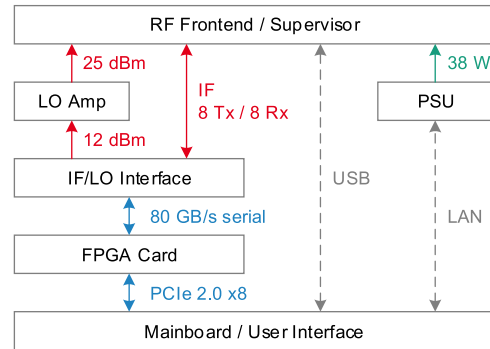

Fig. 8. Block diagram of the realized demonstrator system showing the most relevant analog, high-speed digital, low-speed digital (dashed), and dc interconnects.

angles, absorbing material within the enclosure, and choice of radome reflectivity.

IV. DEMONSTRATOR HARDWARE

A. Overview

In order to verify the proposed aperture and system concept, the demonstrator shown in Fig. 7 was developed. All parts are mounted in a standard 19-in mobile rack to facilitate field testing. According to the top-level block diagram in Fig. 8, it consists of the following main parts that are presented in this section.

The top part (black enclosure) houses the RF front end on a manually steerable mount, containing eight transmitter and eight receiver paths, and some additional monitoring and control circuitry (Section IV-B).

The rack itself contains a standard personal computer with additional custom baseband processing hardware, providing signal conditioning, timing, local oscillator (LO) generation, and data acquisition (Section IV-C). It runs the analysis and control software that does most of the high-level processing, visualization, and user interfacing. The host computer is connected to a touchscreen mounted on top of the rack, opposite the RF aperture.

B. RF Front End

Fig. 9 shows the front view of the RF front end after removal of the white radome seen before, along with a more detailed block diagram of the included components. The basic architecture of the active part is typical of a monostatic digital radar system. It consists of a Tx path featuring an upconverting mixer with an additional medium power amplifier (MPA) and an Rx path comprising an LNA integrated with a downconverting mixer [38]–[41]. The LO is distributed to all 16 channels at $1/12$ of the operating frequency (i.e., 7–9 GHz) and subsequently multiplied on-chip [42].

The upconverter is realized as a double-balanced IQ mixer with an external 90° hybrid, resulting in single-sideband

operation over an IF range of approximately 90–210 MHz. Similarly, the downconverter is based on a single-ended IQ mixer with the same external hybrid, thus operating as an image-reject mixer in the same frequency range.

All active components are fabricated as monolithic microwave integrated circuits (MMICs) on a 50-nm node of the Fraunhofer IAF InAlAs/InGaA-based depletion-type metamorphic high-electron-mobility transistor (mHEMT) technology and packaged in split-block modules with WR-10 waveguide flanges. The resulting combination of very low noise with a high operating bandwidth and output power is particularly beneficial to radar systems based on the hybrid aperture concept presented in this work. Table II summarizes the typical active component specifications that are most relevant from a system designer's point of view.

The realized antenna elements can be seen in the center part of the left of Fig. 9. Relating to Fig. 1, the x-axis (i.e., MIMO dimension) is aligned with the vertical axis in the image plane. The eight Tx antennas with vertical flaring/horn structures are mounted in the top part at a vertical distance of 20 mm; the eight Rx LWAs are integrated into a single brass module with a corresponding element distance of 2.5 mm. Due to the geometric dimension of the waveguide flanges, a fan-in structure is added between the MPA outputs and the antenna inputs. The symmetric fan-out structure with modular waveguide absorbers was included to provide a simple way of performing two-port measurements on the manufactured antenna prototype and could have been included in the central block. In order to minimize conduction losses, the surface finishing of the RF components is a very thin layer of galvanized gold.

LO distribution, dc supply, and the constant supervision of the active components are integrated on a printed circuit board in the back of the enclosure (not shown). The IF signals are routed via SMA cables from the RF front end to the baseband processing unit that is described in Section IV-C.

C. Baseband Processing

The main components in the baseband signal processing chain are shown in Fig. 6 in the context of the system transfer function. Due to the single-sideband or image-reject operation

This article has been accepted for inclusion in a future issue of this journal. Content is final as presented, with the exception of pagination.

10   IEEE TRANSACTIONS ON MICROWAVE THEORY AND TECHNIQUES
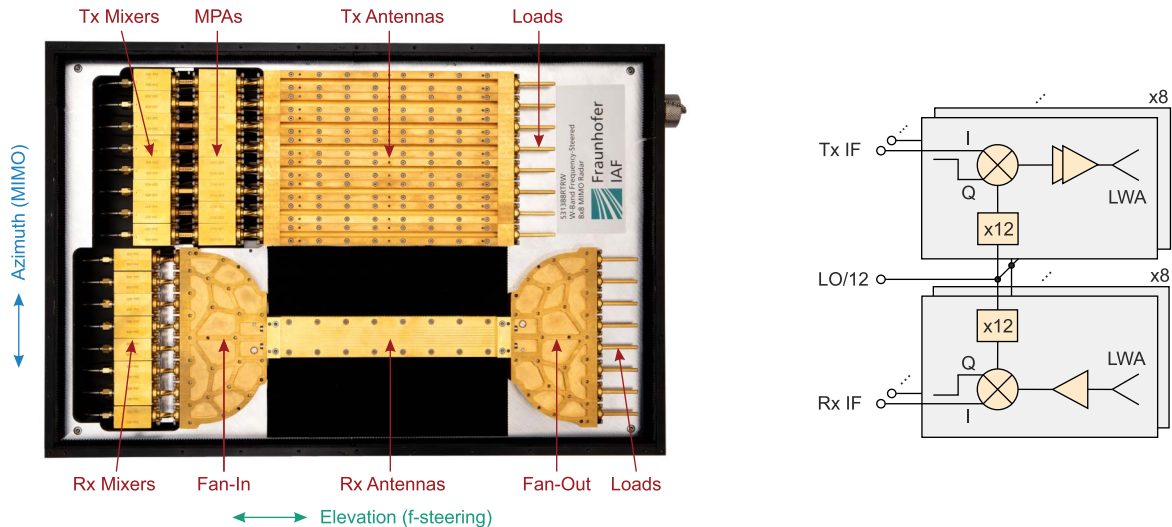

Fig. 9. Left: photograph of the RF front end without radome. The top half consists of eight Tx chains (from left to right: IQ upconverter, MPA, antenna, and absorber). Eight receiver paths (IQ downconverter, fan-in, integrated antenna array, fan-out, and absorbers) are placed in the bottom half of the enclosure. Right: block diagram of the RF front end, additionally showing hybrids for single-sideband operation and the LO distribution network integrated in the back of the enclosure (not shown).

TABLE II
TYPICAL RF FRONT-END SPECIFICATIONS

# Transmit channels		8	
# Receive channels		8	
Lower operating frequency		85	GHz
Upper operating frequency		105	GHz
Tx	Conversion gain (SSB)	15	dB
	Saturated output power	15	dBm
	Output P1dB	11	dBm
	LO rejection	15	dB
	Sideband suppression	20	dB
Rx	Noise figure	3	dB
	Conversion gain (IR)	12	dB
	Image rejection	20	dB

of the front ends, there are eight digital-to-analog converters (DACs) and eight analog-to-digital converters (ADCs), all synchronized with a deterministic latency using the JESD204B protocol. The DACs operate with an oversampling factor 4, enabling a simple design of the reconstruction filter. The receive path consists of a ten-stage Chebyshev filter with a passband of 95–220 MHz, followed by an LNA with a fixed gain of 32 dB and two variable amplifier stages with up to 60 dB additional gain.

The LO signal is generated by a commercial phase-locked loop (PLL) in combination with a wideband voltage-controlled oscillator (VCO) and a loop filter with a bandwidth of 450 kHz, which is a compromise between phase noise performance and switching speed. As demonstrated by Schindler *et al.* [37], this tradeoff could easily be relaxed by a combination of two PLLs with a suitable interleaving logic in applications where switching speed is crucial. The VCO output signal is preamplified on the interface board to a level of approximately 12 dBm and routed to an external power amplifier for achieving the drive level required by the distribution system integrated in the RF front end.

The custom LO/IF interface is integrated in a compact 5.25-in ATX enclosure and installed in a rack-mount personal computer, together with a commercial field-programmable gate array (FPGA) evaluation board (Xilinx VC707). The connection between the interface and the FPGA board is based on the widely used mezzanine system, comprising an 80 Gbit/s full-duplex serial link to the converters as well as a number of general-purpose signals controlling, e.g., the register configuration and the stepping of the LO PLL.

To provide maximum flexibility during algorithm development and prototyping, the FPGA is tasked only with the most timing-critical parts of the baseband processing, i.e., the coherent buffering, transmission, reception, and storage of the IF time-domain samples as well as the carrier stepping. It is basically transparent to all other configuration commands that are internally dispatched by a lightweight soft-core processor. Data transfer from and to the FPGA is done via direct memory access over the PCI Express bus of the host computer. Although no preprocessing (e.g., cyclic prefix handling or the first level of (inverse) fast Fourier transforms) is done on the FPGA, the fast digital interface in conjunction with an efficient user-level application enables soft real-time operation of the demonstrator (e.g., 6–30 frames/s, depending on the choice of processing parameters) while maintaining full access to all steps in the processing chain and entirely avoiding the intricacies of fixed-point arithmetic during the evaluation of the system concept.

A typical set of baseband parameters used to obtain the results presented in Section V is given in Table III. As briefly mentioned in Section III-B, the number of nonzero subcarriers N_{nzsc} per subsymbol differs from the total number of subcarriers N_s in the standard OFDM model due to the need for guard subcarriers on the one hand (filter design and ac coupling) and additionally needs to be halved as a result of the single-sideband operation. To obtain a continuous sampling

This article has been accepted for inclusion in a future issue of this journal. Content is final as presented, with the exception of pagination.

SCHNEIDER *et al.*: HYBRID BEAM-STEERING OFDM-MIMO RADAR

11

TABLE III

TYPICAL SET OF BASEBAND PARAMETERS

| Parameter	Description	Value
N_s	Subcarriers per sub-symbol	5120
N_{nzsc}	Non-zero subcarriers per sub-symbol	1008
N_k	Total number of carrier steps	200
f_s	Sampling rate (w/o oversampling)	500 MHz
β	Subcarrier spacing	97.7 kHz
K	Number of sub-symbols per ϑ-sector	1 to 32
N_ϑ	Number of ϑ-sectors	$N_k - K + 1$
B_s	Sub-symbol (IF) bandwidth	98.3 MHz
B	Coherent integration bandwidth	$K B_s$
δR	Range resolution	see Sect. II-C
R_{max}	Unambiguous range	192 m
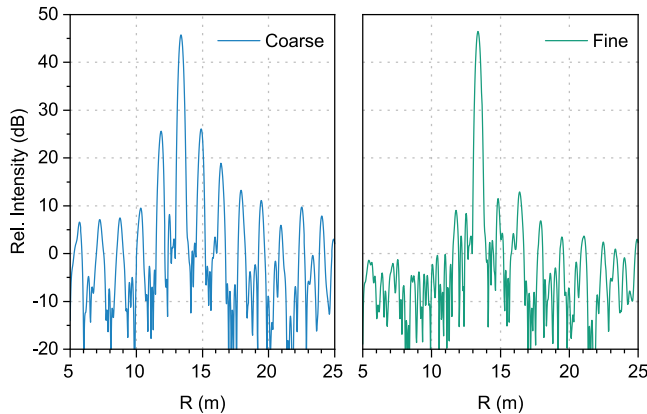
Fig. 10. Result of SC-OFDM range compression combining ten subsymbols. The profiles correspond to a single reflector after a coarse (left) and fine (right) optimization of the IF delay parameter τ in combination with a loopback compensation.

of the channel function, the carrier step B_s is related to N_{nzsc}, as given in Table III.

V. SYSTEM VERIFICATION

In this section, the results of several measurements taken with the demonstrator system are presented. The first part is based on three simple setups intended to verify the theoretical analysis of the hybrid aperture as well as the proposed calibration routines (Sections V-A–V-C). In the second part, three more complex imaging situations are investigated to convey an impression of the system's capabilities in real-world scenarios (Section V-D).

The reference targets used in this section are standard trihedral reflectors with an edge length of 5 cm, corresponding to a boresight cross section of approximately 3 dBm^2 in the W-band.

A. IF Calibration

The IF calibration based on the error model (28) discussed in Section III-D serves the purpose of suppressing artificial sidelobes occurring due to noncontinuous channel functions. Without any calibration, the radar data after range compression are unusable, so this case is not depicted here. After incorporating the results of the IF loopback measurement,
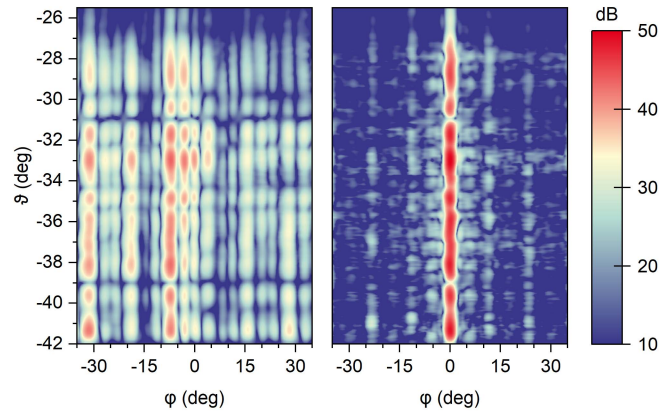

Fig. 11. Cross-range image of a number of trihedral reflectors mounted on a vertical post (see Fig. 14) at a distance of approximately 13 m, obtained before (left) and after (right) application of the proposed MIMO calibration routine.

the delay parameter τ is first chosen as an integer multiple of the inverse sampling frequency based on estimations of the internal processing delays. This coarse calibration can be very efficiently implemented as a cyclic shift in the receive buffer and is shown in the left of Fig. 10 for a single trihedral reflector placed at about 13.4 m. The target position is correctly reconstructed, but the remaining sidelobes are still clearly visible. The right of Fig. 10 is based on the same raw data, but after continuous optimization of τ as explained in Section III-D. As a result, the artificial sidelobes are significantly suppressed. Note that a Hamming window is applied to the data in the range dimension in order to suppress the sampling-based sidelobes that would otherwise mask the IF artifacts.

B. RF Calibration

The proposed RF calibration routine (31) is realized by moving a number of strong reflectors in the $\varphi = 0$ plane and automatically extracting the RF phases for the detected targets until the available elevation interval is fully covered. Note that a high (i.e., phase-based) precision is not necessary during this process, as the results of all elevation sectors are mutually independent of each other, which significantly reduces the manual effort.

For verification purposes, a single measurement is taken of a number of trihedral reflectors mounted on a vertical post centered in front of the aperture at a distance of approximately 13 m, equidistantly spaced 35 cm (see inset of Fig. 14). This should, in theory, yield a straight line at $\varphi = 0$, possibly with some interference effects due to neighboring reflectors. Beside the obvious focusing of the energy, an important criterion for the success of the calibration is the continuity of the resulting image along the elevation dimension, as there is no interaction between the sectors. The right of Fig. 11 verifies that the proposed method achieves an MIMO calibration of high quality suitable for the targeted imaging applications.
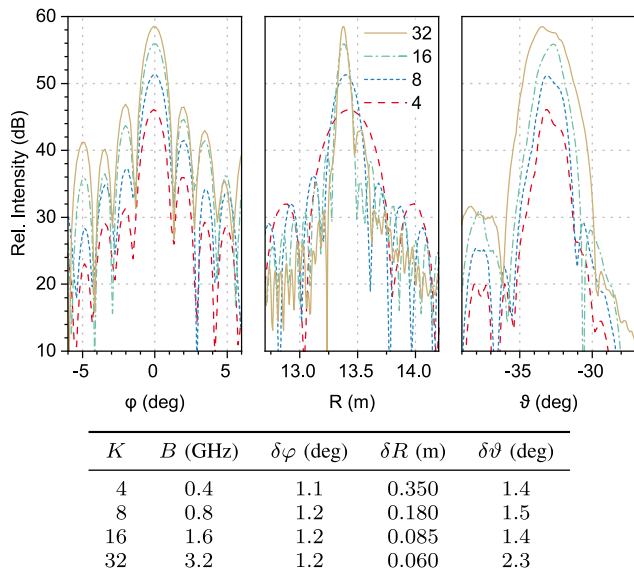
This article has been accepted for inclusion in a future issue of this journal. Content is final as presented, with the exception of pagination.

12   IEEE TRANSACTIONS ON MICROWAVE THEORY AND TECHNIQUES

K	B (GHz)	$\delta\varphi$ (deg)	δR (m)	$\delta\vartheta$ (deg)
4	0.4	1.1	0.350	1.4
8	0.8	1.2	0.180	1.5
16	1.6	1.2	0.085	1.4
32	3.2	1.2	0.060	2.3

Fig. 12.   Top: azimuth, range, and elevation cuts of a radar image of a single trihedral reflector. The integration bandwidth per angle is varied from $K = 4$ to 32 subsymbols or from 0.4 to 3.2 GHz. Bottom: estimated resolutions given by the FWHM extracted from the graphs.

C. Resolution

To demonstrate the influence of the coherent integration bandwidth B on the imaging resolution of the system as predicted in Fig. 4, a measurement of a single trihedral reflector is taken and processed for various values of K. The result is visualized in Fig. 12, which consists of three orthogonal cuts through the reconstructed image.

As expected, the azimuth resolution does not change with B, while the range resolution is proportional to $1/B$ for small values of B and flattens for large B due to the incomplete coverage explained in Section II-C. The elevation resolution, on the other hand, remains almost constant until the effective broadening of the antenna pattern shown in the inset of Fig. 4 becomes relevant for large B. The estimated (minimum) opening angle of the antennas in the elevation plane is slightly larger than predicted by the simulation, which can be attributed to the relatively small ratio of measurement range and Fraunhofer distance at 13.5 m [21]. Also, note that the observed increase of the peak value by 6 dB (or 3 dB with respect to the thermal noise floor) in the case of full coherency is a consequence of the processing gain of the Fourier transform as the number of available subcarriers doubles in each step. It has not been compensated here as it improves the legibility of the plots by shifting the individual curves.

D. Complex Scenes

In Fig. 13, a rectangular, empty parking lot with a metal fence is used as a test scene that primarily extends in range and azimuth direction. An elevation cut parallel to the ground is depicted in the bottom part of the figure, resolving a number of metal posts as well as the staircase behind the left part of the rear fence. The building in the center of the photograph also
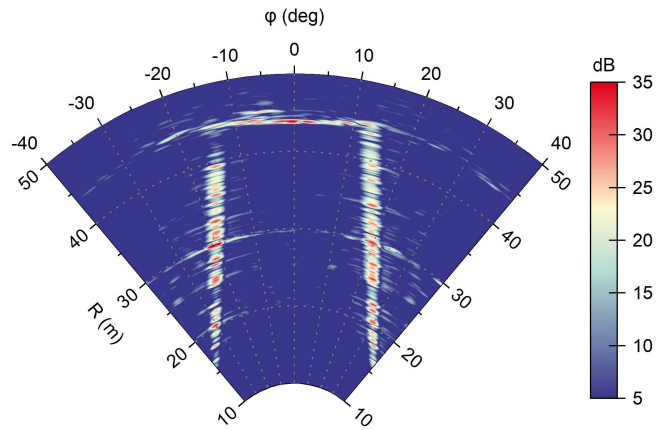

Fig. 13.   Photograph (top) and elevation cut of a radar image (bottom) showing an 18 m × 45 m parking deck with a metal fence. Several individual posts of the fence are resolved as individual reflectors.
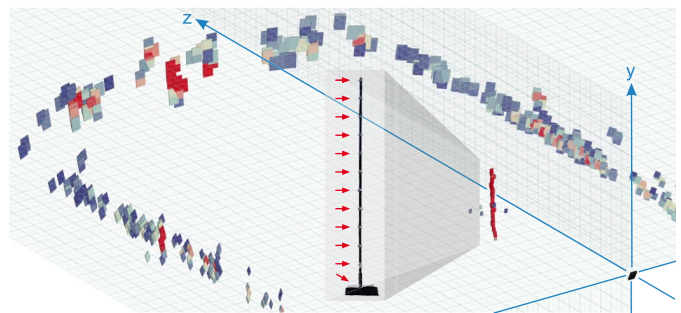

Fig. 14.   3-D target plot of the parking lot from Fig. 13 with an additional vertical pole at a range of 13 m supporting 12 trihedral reflectors equidistantly spaced 35 cm. The RF front end (origin of the coordinate system, approximately 1.7 m above the ground) is drawn to scale in the bottom right corner. Inset: photograph of the pole with arrows marking the positions of the reflectors.

generates a distinct reflection at a range of 70 m not shown in the radar image.

The same parking deck is shown in Fig. 14 with an additional target that extends along the elevation direction (see the inset). The 3-D plot is generated by applying a standard peak search kernel considering the eight nearest neighbors to the radar data ρ' after thresholding.

An arrangement of trihedral reflectors extending in the azimuth and elevation direction is shown in Fig. 15 to illustrate the cross-range imaging capabilities of the hybrid aperture concept. At a range of 13 m, several closely spaced targets are distributed at the center and near the edge of the aperture. The resulting image demonstrates both the achieved resolution

This article has been accepted for inclusion in a future issue of this journal. Content is final as presented, with the exception of pagination.

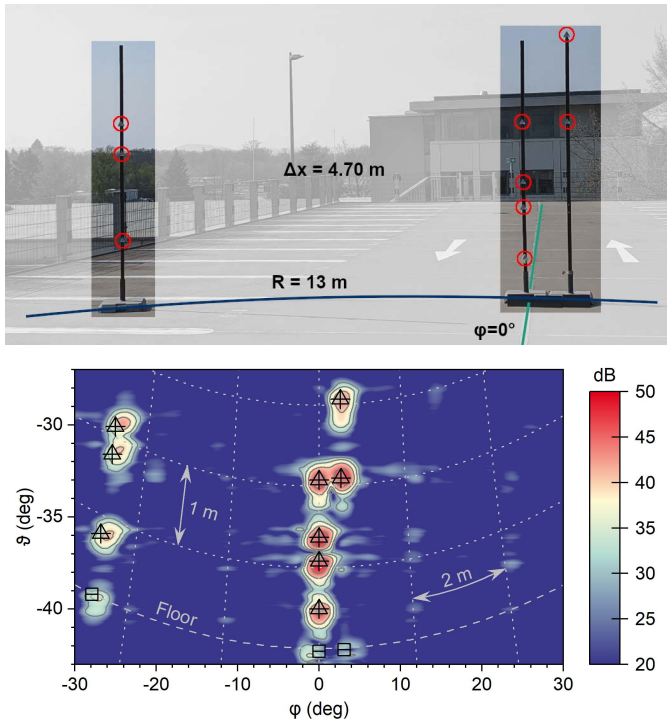SCHNEIDER *et al.*: HYBRID BEAM-STEERING OFDM-MIMO RADAR

13

Fig. 15. Photograph (top) and measurement (bottom) of an arrangement of trihedral reflectors illustrating the cross-range imaging performance of the system. Triangles mark the ground truth of the reflectors; squares denote the position of the stands. The (solid) isolines are spaced 5 dB. The grid lines are guides to the eye in "parking deck coordinates" while the overall mapping is an equirectangular projection of the partial sphere shown in Fig. 1, tilted toward boresight.
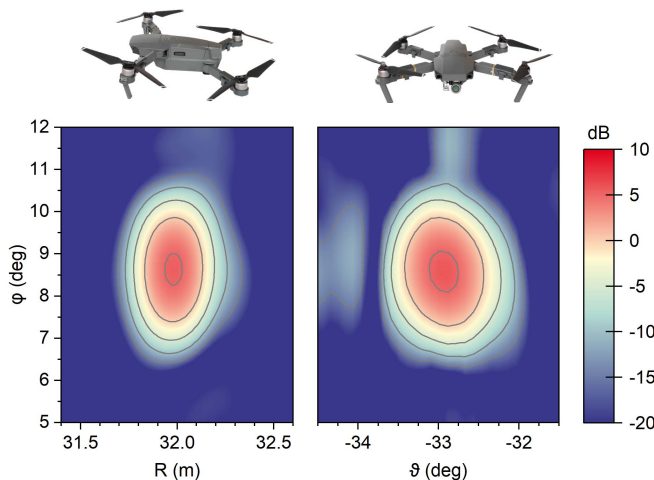

Fig. 16. Cuts of the radar image of a small commercial drone (33 cm × 25 cm × 9 cm, pictures not to scale) hovering at a distance of 32 m, approximately 10 m above the ground. The isolines are spaced 5 dB.

as well as the antenna pattern in the azimuth direction shown in the right of Fig. 3.

To give an example of the energy distribution received from a small, moving target, we conclude this section by presenting a partial radar image of the parking lot with a small commercial drone (DJI Mavic Pro 2) hovering at a distance of 32 m, approximately 10 m above the ground (see Fig. 16).

VI. CONCLUSION

With this article, we have aimed at answering the following set of research questions.

1) How can broadband radar systems benefit the most from the tradeoff between bandwidth and additional MIMO channels enabled by the hybrid aperture concept?
2) What specific properties does a highly directive, hybrid aperture have regarding the interaction of resolutions, and how can these be tuned during design and operation?
3) What challenges and opportunities come with the integration of such a hybrid aperture into an SC-OFDM radar, with a special focus on signal processing and calibration?

Our proposed answer to the first two questions is the design and analysis of an aperture based on the integration of a recent form of LWAs in the transmit and receive paths of a tightly spaced, 1-D MIMO array. A single, all-electronic measurement performed with the resulting system features a 3-D Fourier resolution that has, to our knowledge, not been demonstrated before with a comparably small number of active channels.

By presenting a viable path to the seamless integration of the proposed aperture into an SC-OFDM radar, we hope to have proven the potential of the concept in the context of future generations of broadband digital radar systems. We have shown in which ways SC-OFDM and the hybrid aperture concept benefit from each other (bandwidth subdivision) and successfully addressed the arising challenges regarding calibration.

The proposed concepts and algorithms have been verified by implementation in a self-contained demonstrator that shows the expected performance in various scenes composed of reference targets as well as real-world objects and surroundings.

VII. OUTLOOK

There are a number of aspects of the current system concept that constitute interesting starting points for future research.

From a system integrator's point of view, the hybrid aperture concept should be investigated when combined with a more situation-aware high-level signal processing. This includes, but is not limited to, classic super-resolution techniques, such as Unitary ESPRIT [43] and MUSIC [44], sparse reconstruction [20], [45], deconvolution of the antenna pattern in elevation direction using algorithms like CLEAN [46], as well as the addition of tracking and classification units. Finally, though mostly an implementation aspect, the efficient distribution of processing steps on the available computing platforms (CPU, FPGA, and graphics processor) can be exploited to achieve hard real-time capabilities to the degree required by the application.

On the RF hardware side, we see potential in the transfer of the antenna concept to alternative manufacturing strategies based, e.g., on wafer-scale processing [47], [48]. In combination with a transition to higher operating frequencies, a large absolute bandwidth can be used (e.g., 100 GHz in the Y-band [49]) that could lead to an increased elevation coverage and/or range resolution. Of course, improving the azimuth

resolution at the expense of an increased sidelobe level is always an option via the synthesis of sparse arrays [10].

In the medium future, the ongoing advances in the fields of converters and system-on-chip solutions [19] will eventually allow for complete decoupling of the elevation sectors by sampling the required number of subsymbols cost-efficiently in a single carrier step, turning SC-OFDM into a form of "stepped-elevation OFDM," thus fully eliminating the former's remaining shortcomings regarding the slow-time phase progression between subsymbols.

References

[1] J. Dickmann *et al.*, "Making bertha see even more: Radar contribution," *IEEE Access*, vol. 3, pp. 1233–1247, Jul. 2015.

[2] D. Meier *et al.*, "Propagation of millimeter waves in composite materials," *IEEE Trans. Antennas Propag.*, vol. 68, no. 4, pp. 3080–3093, Apr. 2020.

[3] T. Jaeschke, C. Bredendiek, and N. Pohl, "A 240 GHz ultra-wideband FMCW radar system with on-chip antennas for high resolution radar imaging," in *IEEE MTT-S Int. Microw. Symp. Dig.*, Jun. 2013, pp. 1–4.

[4] N. Pohl, T. Jaeschke, and K. Aufinger, "An ultra-wideband 80 GHz FMCW radar system using a SiGe bipolar transceiver chip stabilized by a fractional-N PLL synthesizer," *IEEE Trans. Microw. Theory Techn.*, vol. 60, no. 3, pp. 757–765, Mar. 2012.

[5] S. Yuan, A. Trasser, and H. Schumacher, "56 GHz bandwidth FMCW radar sensor with on-chip antennas in SiGe BiCMOS," in *IEEE MTT-S Int. Microw. Symp. Dig.*, Jun. 2014, pp. 1–4.

[6] T. Spreng, S. Yuan, V. Valenta, H. Schumacher, U. Siart, and V. Ziegler, "Wideband 120 GHz to 140 GHz MIMO radar: System design and imaging results," in *Proc. Eur. Microw. Conf. (EuMC)*, Sep. 2015, pp. 430–433.

[7] H. Wilden, J. Klare, A. Froehlich, and M. Krist, "MIRA-CLE, an experimental MIMO radar in Ka band," in *Proc. Eur. Conf. Synth. Apert. Radar (EUSAR)*, Jun. 2010, pp. 382–385.

[8] D. Bleh *et al.*, "W-band time-domain multiplexing FMCW MIMO radar for far-field 3-D imaging," *IEEE Trans. Microw. Theory Techn.*, vol. 65, no. 9, pp. 3474–3484, Sep. 2017.

[9] W. Johannes, M. Caris, and S. Stanko, "94 GHz radar used for perimeter surveillance with wide target clarification," in *Proc. 21st Int. Radar Symp. (IRS)*, Oct. 2020, pp. 15–18.

[10] R. Feger, C. Wagner, S. Schuster, S. Scheiblhofer, H. Jager, and A. Stelzer, "A 77-GHz FMCW MIMO radar based on an SiGe single-chip transceiver," *IEEE Trans. Microw. Theory Techn.*, vol. 57, no. 5, pp. 1020–1035, May 2009.

[11] S. S. Ahmed, A. Schiessl, and L.-P. Schmidt, "A novel fully electronic active real-time imager based on a planar multistatic sparse array," *IEEE Trans. Microw. Theory Techn.*, vol. 59, no. 12, pp. 3567–3576, Dec. 2011.

[12] S. Kueppers, H. Cetinkaya, R. Herschel, and N. Pohl, "A compact 24 × 24 channel MIMO FMCW radar system using a substrate integrated waveguide-based reference distribution backplane," *IEEE Trans. Microw. Theory Techn.*, vol. 68, no. 6, pp. 2124–2133, Jun. 2020.

[13] S. Yang and H. Ling, "Application of a microstrip leaky wave antenna for range-azimuth tracking of humans," *IEEE Geosci. Remote Sens. Lett.*, vol. 10, no. 6, pp. 1384–1388, Nov. 2013.

[14] A. Hommes, A. Shoykhetbrod, and N. Pohl, "A fast tracking 60 GHz radar using a frequency scanning antenna," in *Proc. 39th Int. Conf. Infr., Millim., THz Waves (IRMMW-THz)*, Sep. 2014, pp. 1–2.

[15] T. Geibig, A. Shoykhetbrod, A. Hommes, R. Herschel, and N. Pohl, "Compact 3D imaging radar based on FMCW driven frequency-scanning antennas," in *Proc. IEEE Radar Conf. (RadarConf)*, May 2016, pp. 1–5.

[16] A. Orth, P. Kwiatkowski, and N. Pohl, "A novel approach for a MIMO FMCW radar system with frequency steered antennas for 3D target localization," in *Proc. Eur. Radar Conf. (EuRAD)*, Oct. 2019, pp. 37–40.

[17] A. Shoykhetbrod, H. Cetinkaya, and S. Nowok, "Measurement-based performance investigation of a hybrid MIMO-frequency scanning radar," in *IEEE MTT-S Int. Microw. Symp. Dig.*, Aug. 2020, pp. 1251–1254.

[18] G. Hakobyan and B. Yang, "High-performance automotive radar: A review of signal processing algorithms and modulation schemes," *IEEE Signal Process. Mag.*, vol. 36, no. 5, pp. 32–44, Sep. 2019.

[19] B. Farley *et al.*, "A programmable RFSoC in 16 nm FinFET technology for wideband communications," in *Proc. IEEE Asian Solid-State Circuits Conf. (A-SSCC)*, Nov. 2017, pp. 1–4.

[20] C. Knill, B. Schweizer, and C. Waldschmidt, "Interference-robust processing of OFDM radar signals using compressed sensing," *IEEE Sensors Lett.*, vol. 4, no. 4, pp. 1–4, Apr. 2020.

[21] D. A. Schneider, M. Rösch, A. Tessmann, and T. Zwick, "A low-loss W-band frequency-scanning antenna for wideband multichannel radar applications," *IEEE Antennas Wireless Propag. Lett.*, vol. 18, no. 4, pp. 806–810, Apr. 2019.

[22] H. Krim and M. Viberg, "Two decades of array signal processing research: The parametric approach," *IEEE Signal Process. Mag.*, vol. 13, no. 4, pp. 67–94, Jul. 1996.

[23] B. J. Donnet and I. D. Longstaff, "Combining MIMO radar with OFDM communications," in *Proc. Eur. Radar Conf. (EuRAD)*, Sep. 2006, pp. 37–40.

[24] C. Sturm, T. Zwick, and W. Wiesbeck, "An OFDM system concept for joint radar and communications operations," in *Proc. IEEE 69th Veh. Technol. Conf. (VTC Spring)*, Apr. 2009, pp. 1–5.

[25] N. Levanon, "Multifrequency complementary phase-coded radar signal," *IEE Proc.-Radar, Sonar Navigat.*, vol. 147, no. 6, pp. 276–284, Dec. 2000

[26] C. Sturm, E. Pancera, T. Zwick, and W. Wiesbeck, "A novel approach to OFDM radar processing," in *Proc. IEEE Radar Conf.*, May 2009, pp. 1–4.

[27] B. Nuss, L. G. de Oliveira, and T. Zwick, "Frequency comb MIMO OFDM radar with nonequidistant subcarrier interleaving," *IEEE Microw. Wireless Compon. Lett.*, vol. 30, no. 12, pp. 1209–1212, Dec. 2020.

[28] C. Pfeffer, R. Feger, and A. Stelzer, "A stepped-carrier 77-GHz OFDM MIMO radar system with 4 GHz bandwidth," in *Proc. Eur. Radar Conf.*, Sep. 2015, pp. 97–100.

[29] B. Schweizer, C. Knill, D. Schindler, and C. Waldschmidt, "Stepped-carrier OFDM-radar processing scheme to retrieve high-resolution range-velocity profile at low sampling rate," *IEEE Trans. Microw. Theory Techn.*, vol. 66, no. 3, pp. 1610–1618, Mar. 2018.

[30] B. Schweizer, D. Schindler, C. Knill, J. Hasch, and C. Waldschmidt, "Expanding the unambiguous velocity limitation of the stepped-carrier OFDM radar scheme," in *Proc. Eur. Radar Conf. (EuRAD)*, Sep. 2018, pp. 22–25.

[31] S. H. Han and J. H. Lee, "An overview of peak-to-average power ratio reduction techniques for multicarrier transmission," *IEEE Wireless Commun.*, vol. 12, no. 2, pp. 56–65, Apr. 2005.

[32] V. Winkler, "Range Doppler detection for automotive FMCW radars," in *Proc. Eur. Radar Conf.*, Oct. 2007, pp. 1445–1448.

[33] C. Knill, F. Embacher, B. Schweizer, S. Stephany, and C. Waldschmidt, "Coded OFDM waveforms for MIMO radars," *IEEE Trans. Veh. Technol.*, early access, Apr. 15, 2021, doi: 10.1109/TVT.2021.3073268.

[34] C. Sturm, Y. L. Sit, M. Braun, and T. Zwick, "Spectrally interleaved multi-carrier signals for radar network applications and multi-input multi-output radar," *IET Radar Sonar Navigat.*, vol. 7, no. 3, pp. 261–269, Mar. 2013.

[35] G. Hakobyan, M. Ulrich, and B. Yang, "OFDM-MIMO radar with optimized nonequidistant subcarrier interleaving," *IEEE Trans. Aerosp. Electron. Syst.*, vol. 56, no. 1, pp. 572–584, Feb. 2020.

[36] T. Multerer, U. Prechtel, M. Vossiek, and V. Ziegler, "Systematic phase correction for direction-of-arrival estimation in spectrally interleaved OFDM MIMO radar," *IEEE Trans. Microw. Theory Techn.*, vol. 67, no. 11, pp. 4570–4577, Nov. 2019.

[37] D. Schindler, B. Schweizer, C. Knill, J. Hasch, and C. Waldschmidt, "An integrated stepped-carrier OFDM MIMO radar utilizing a novel fast frequency step generator for automotive applications," *IEEE Trans. Microw. Theory Techn.*, vol. 67, no. 11, pp. 4559–4569, Nov. 2019.

[38] A. Tessmann *et al.*, "A coplanar 94 GHz low-noise amplifier MMIC using 0.07 μm metamorphic cascode HEMTs," in *IEEE MTT-S Int. Microw. Symp. Dig.*, Jun. 2003, pp. 1581–1584.

[39] A. Tessmann, A. Leuther, C. Schwoerer, and H. Massler, "Metamorphic 94 GHz power amplifier MMICs," in *IEEE MTT-S Int. Microw. Symp. Dig.*, Jun. 2005, pp. 1579–1582.

[40] A. Tessmann *et al.*, "A compact W-band dual-channel receiver module," in *IEEE MTT-S Int. Microw. Symp. Dig.*, Jun. 2006, pp. 85–88.

[41] M. Rösch *et al.*, "Compact W-band receiver module on hybrid liquid crystal polymer board," in *Proc. 46th Eur. Microw. Conf. (EuMC)*, Oct. 2016, pp. 1517–1520.

[42] U. J. Lewark *et al.*, "Ultra-broadband W-band frequency multiplier-by-twelve MMIC," in *Proc. 10th Eur. Microw. Integr. Circuits Conf. (EuMIC)*, Sep. 2015, pp. 5–8.

[43] M. Haardt and J. A. Nossek, "Unitary ESPRIT: How to obtain increased estimation accuracy with a reduced computational burden," *IEEE Trans. Signal Process.*, vol. 43, no. 5, pp. 1232–1242, May 1995.

[44] R. O. Schmidt, "Multiple emitter location and signal parameter estimation," *IEEE Trans. Antennas Propag.*, vol. AP-34, no. 3, pp. 276–280, Mar. 1986.

[45] M. Rossi, A. M. Haimovich, and Y. C. Eldar, "Spatial compressive sensing for MIMO radar," *IEEE Trans. Signal Process.*, vol. 62, no. 2, pp. 419–430, Jan. 2014.

[46] J. Högbom, "Aperture synthesis with a non-regular distribution of interferometer baselines," *Astron. Astrophys. Suppl. Ser.*, vol. 15, p. 417, Jun. 1974.

[47] K. Sarabandi, A. Jam, M. Vahidpour, and J. East, "A novel frequency beam-steering antenna array for submillimeter-wave applications," *IEEE Trans. THz Sci. Technol.*, vol. 8, no. 6, pp. 654–665, Nov. 2018.

[48] P. Lu *et al.*, "InP-based THz beam steering leaky-wave antenna," *IEEE Trans. THz Sci. Technol.*, vol. 11, no. 2, pp. 218–230, Mar. 2021.

[49] B. Gashi *et al.*, "Broadband and high-gain 400-GHz InGaAs mHEMT medium-power amplifier S-MMIC," in *IEEE MTT-S Int. Microw. Symp. Dig.*, Aug. 2020, pp. 484–487.

David A. Schneider received the M.Sc. degree in physics from the Technical University of Dortmund, Dortmund, Germany, in 2016. He is currently pursuing the Dr.Ing. degree in electrical engineering in cooperation at Karlsruhe Institute of Technology (KIT), Karlsruhe, Germany.

He has been with the Sensor Systems Group, Fraunhofer Institute for Applied Solid State Physics (IAF), Freiburg, Germany, since 2017. The focus of his research is on concepts and components for future digitally modulated imaging radar.

Markus Rösch received the Dipl.Ing. degree in electrical engineering and the Doctor of Engineering degree in cooperation from Karlsruhe Institute of Technology (KIT), Karlsruhe, Germany, in 2008 and 2013, respectively.

From November 2008 to June 2012, he was a Ph.D. student at the Institut de Radioastronomie millimétrique (IRAM), Saint-Martin-d'Hères, France, where he was developing superconducting kinetic inductance detectors (KID) for millimeter-wave astronomy. Since 2012, he has been a Research Engineer at the Fraunhofer Institute for Applied Solid State Physics (IAF), Freiburg, Germany, where he has been the Head of the Systems Group and responsible for the development of high-frequency radar systems since 2018. His research interest is in the area of millimeter-wave technology, focusing on radar sensors and systems.

Axel Tessmann received the Dipl.Ing. and Dr.Ing. degrees in electrical engineering from the University of Karlsruhe, Karlsruhe, Germany, in 1997 and 2006, respectively.

In 1997, he joined the Microelectronics Department, Fraunhofer Institute for Applied Solid State Physics (IAF), Freiburg, Germany, where he is involved in the development of monolithically integrated circuits and subsystems for high-resolution imaging systems and high-data-rate wireless communication links. He is currently the Group Manager of the Millimeter-Wave Packaging and Subsystem Group, Fraunhofer IAF. His main research interests include the design and packaging of millimeter-wave and submillimeter-wave ICs using high-electron-mobility transistors on GaAs, GaN, and InP as well as circuit simulation and linear and nonlinear device modeling.

Thomas Zwick (Fellow, IEEE) received the Dipl.Ing. (M.S.E.E.) and the Dr.Ing. (Ph.D.E.E.) degrees from the University of Karlsruhe, Karlsruhe, Germany, in 1994 and 1999, respectively.

From 1994 to 2001, he was a Research Assistant at the Institut für Höchstfrequenztechnik und Elektronik (IHE), University of Karlsruhe. In February 2001, he joined the IBM T. J. Watson Research Center, Yorktown Heights, NY, USA, as a Research Staff Member. From October 2004 to September 2007, he was with Siemens AG, Lindau, Germany. During this period, he managed the RF Development Team for automotive radars. In October 2007, he became a Full Professor at Karlsruhe Institute of Technology (KIT), Karlsruhe. He is currently the Director of the Institute of Radio Frequency Engineering and Electronics (IHE), KIT. He is a coeditor of three books, an author or a coauthor of 120 journal articles, and over 400 contributions at international conferences. He holds 15 granted patents. His research topics include wave propagation, stochastic channel modeling, channel measurement techniques, material measurements, microwave techniques, millimeter-wave antenna design, wireless communication, and radar system design.

Dr. Zwick has been a member of the Heidelberg Academy of Sciences and Humanities since 2017. He has also been a member of acatech (German National Academy of Science and Engineering) since 2019. His research team received over ten best paper awards at international conferences. He served on the technical program committees (TPC) of several scientific conferences. He was the General Chair of the International Workshop on Antenna Technology (iWAT2013), Karlsruhe, in 2013, and the IEEE MTT-S International Conference on Microwaves for Intelligent Mobility (ICMIM), Heidelberg, in 2015. He was the TPC Chair of the European Microwave Conference (EuMC) in 2013 and the General TPC Chair of the European Microwave Week (EuMW) in 2017. In 2023, he will be the General Chair of EuMW, Berlin. From 2008 until 2015, he was the President of the Institute for Microwaves and Antennas (IMA). He was selected as a Distinguished IEEE Microwave Lecturer for the term 2013–2015 with his lecture on "QFN Based Packaging Concepts for Millimeter-Wave Transceivers." In 2019, he became the Editor-in-Chief of the IEEE MICROWAVE AND WIRELESS COMPONENTS LETTERS.